

The data generation process is time-consuming since the finite difference method and the reverse time migration for each velocity model are required. To reduce the amount of computation, we set the size of the velocity model to  $512 \times 256$ . To improve the convergence of training and balance the differences in numerical values between the training data and the prediction data, we normalize the input migration images. Many factors can affect the performance of this proposed network, such as the learning rate, batch size, and training epoch. During the training process, data is transmitted to the network in batch form. For data with complex features and large sample differentiation, a larger batch size helps to find the descending direction of gradient more accurately and avoid falling into the local minimum. For the single feature recognition problem with obvious features, the smaller batch is generally adopted to obtain better convergence. During the training stage, the 2D migration images are fed into the neural network in batches with a batch size of 8. It means that for each batch of inputs, the whole neural network will perform complete error backpropagation and gradient calculation, which makes the network achieve better convergence with the same epoch. We use the Adam method (Kingma and Ba, 2014) to optimize the network parameters and set the learning rate to be 0.0001.

We train the network with 100 epochs, and all the 2475 training migration images are processed at each epoch. Fig. 7 shows the convergence curves of the training and validation data sets, where the training loss gradually decreases from 0.0038 to 0.0035, and the validation loss gradually decreases from 0.00363 to 0.00354. As shown in Fig. 7, the error of the training data set has been decreasing, while the error of the validation data set has not decreased since the 38 epoch, which is reasonable because at 38 epoch, the network trained with 2475 training samples has achieved the best

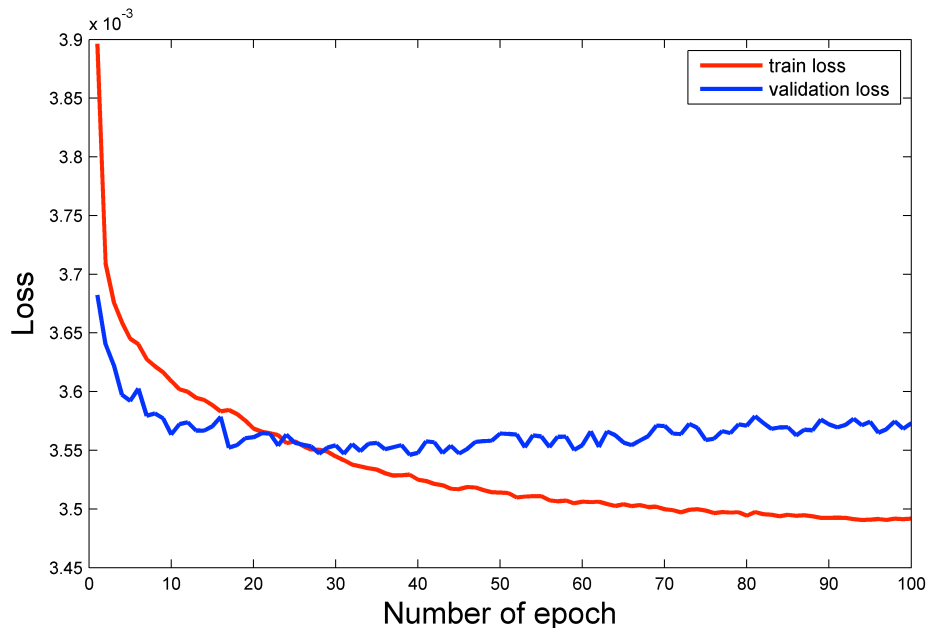


Fig. 7. The training and validation loss decrease with epochs.

set has not decreased since the 38 epoch, which is reasonable because at 38 epoch, the network trained with 2475 training samples has achieved the best effect on the 275 validation samples, and the continuous training may lead to overfitting. We train the network with 100 epochs, and all the 2475 training migration images are processed at each epoch. Fig. 7 shows the convergence curves of the training and validation data sets, where the training loss gradually decreases from 0.0038 to 0.0035, and the validation loss gradually decreases from 0.00363 to 0.00354. As shown in Fig. 7, the error of the training data set has been decreasing, while the error of the validation data set has not decreased since the 38 epoch, which is reasonable because at 38 epoch, the network trained with 2475 training samples has achieved the best effect on the 275 validation samples, and the continuous training may lead to overfitting.

## NUMERICAL EXPERIMENTS AND RESULTS

In this section, we first present one synthetic test on the testing data set. Then we discuss the sensitivity of the proposed method to imaging quality and wavelet frequency.

### **Prediction for the testing data set**

To evaluate the detection performance of our proposed network, we first test it with the migration images generated with seismic data in the absence of noise. The test samples are not included in the training data set and are unknown during the prediction process. Fig. 8a and Fig. 8b show the original velocity model, in which the colored squares denote the karst caves with different scales and different velocities. Fig. 8c and Fig. 8d present the migration imaging results generated from noise free seismic data. Fig. 8e and Fig. 8f are the overlaid images consisting of the predicted karst caves of the trained neural network (red spots) and the migration image (Fig. 8c and Fig. 8d). The prediction results show that when there is noise free, the cavities predicted by our network are in good agreement with the true karst caves in both the locations and scales. The trained network can not only accurately identify the karst caves with obvious beadlike diffraction phenomenon, but also identify the karst caves with weak deep energy and indistinct wave field response characteristics satisfactorily. For the image results of the karst caves at the edge of the model, which show the characteristics of inclined beadlike diffractions, the network can also make accurate recognition. As shown in Fig. 8c, the prediction results of the karst caves distributed around the model tend to remain inclined. Due to the full-receiving observation system, the migration imaging result with the karst cave located at the edge of the model shows slanted beadlike diffraction. For the conventional vertical distribution of beadlike diffraction characteristics, the neural

network can identify and distinguish the karst caves accurately. The advantage of the neural network over manual recognition is that it can not only identify the karst caves accurately but also predict the locations and the scales of the karst caves with high accuracy. The loss function is calculated pixel by pixel and is affected by the accuracy and precision of karst cave identification. Once the training stage is completed, the prediction results will gradually converge to the true locations of the karst caves. Therefore, the trained neural network can not only identify karst caves but also describe their locations accurately.

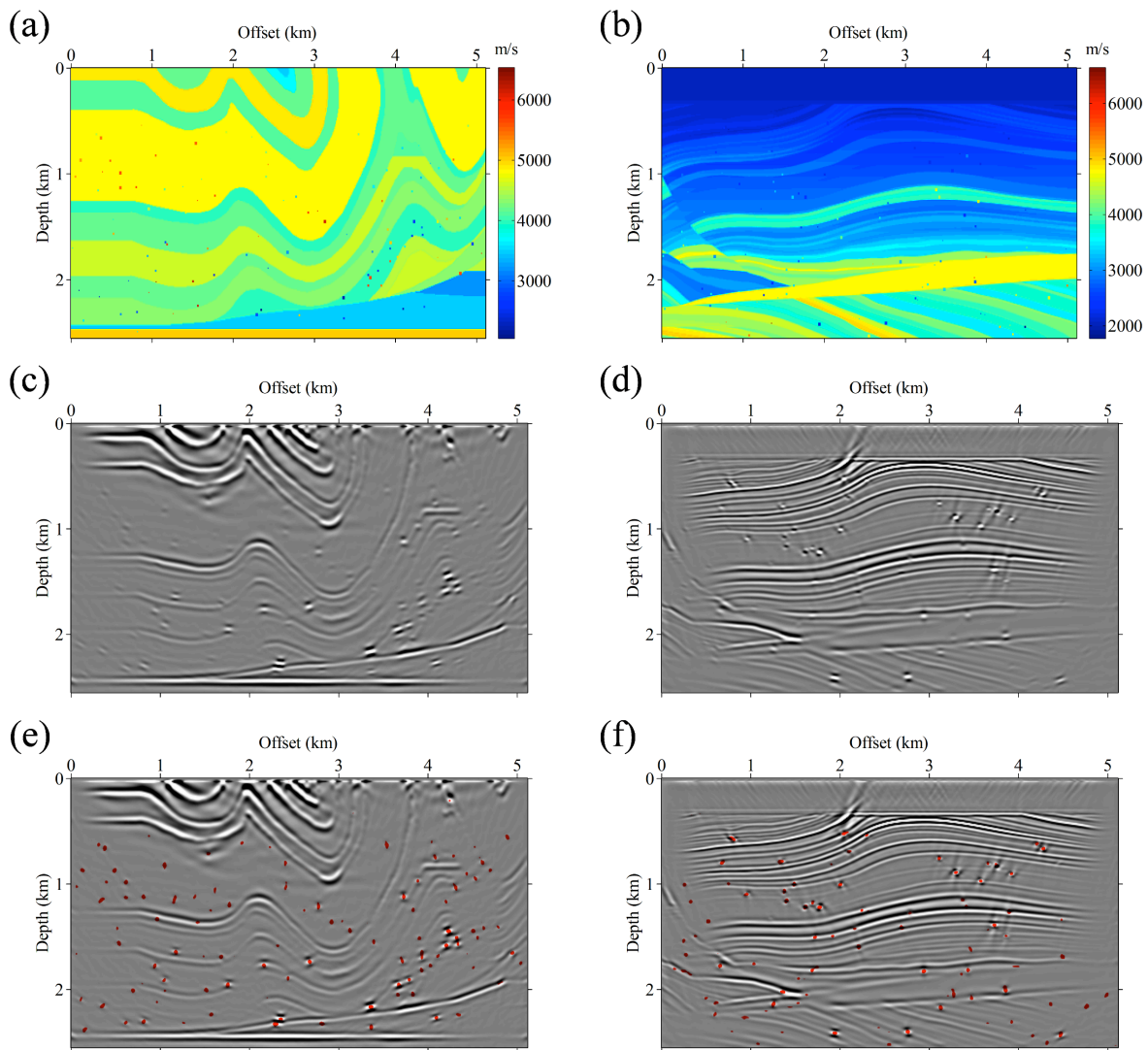


Fig. 8. The prediction results on the testing data set. (a) The velocity model with karst caves based on the section of the BP 2.5D model. (b) The velocity model with karst caves based on the section of the Marmousi model. (c-d) The corresponding migration image of (a-b). (d-f) The overlaid image consists of the predicted karst caves of the trained neural network (red spots) and migration image (c-d).

## Sensitivity tests on the imaging quality and wavelet frequency

We further test the influence of migration noise on the predictions. We apply the trained network to the new testing data generated with the same process as the training data generation. Note that the migration images of the training data set are generated from shot records with random noise. Fig. 9a and Fig. 9b are the same velocity models as in Fig. 8a and Fig. 8b.

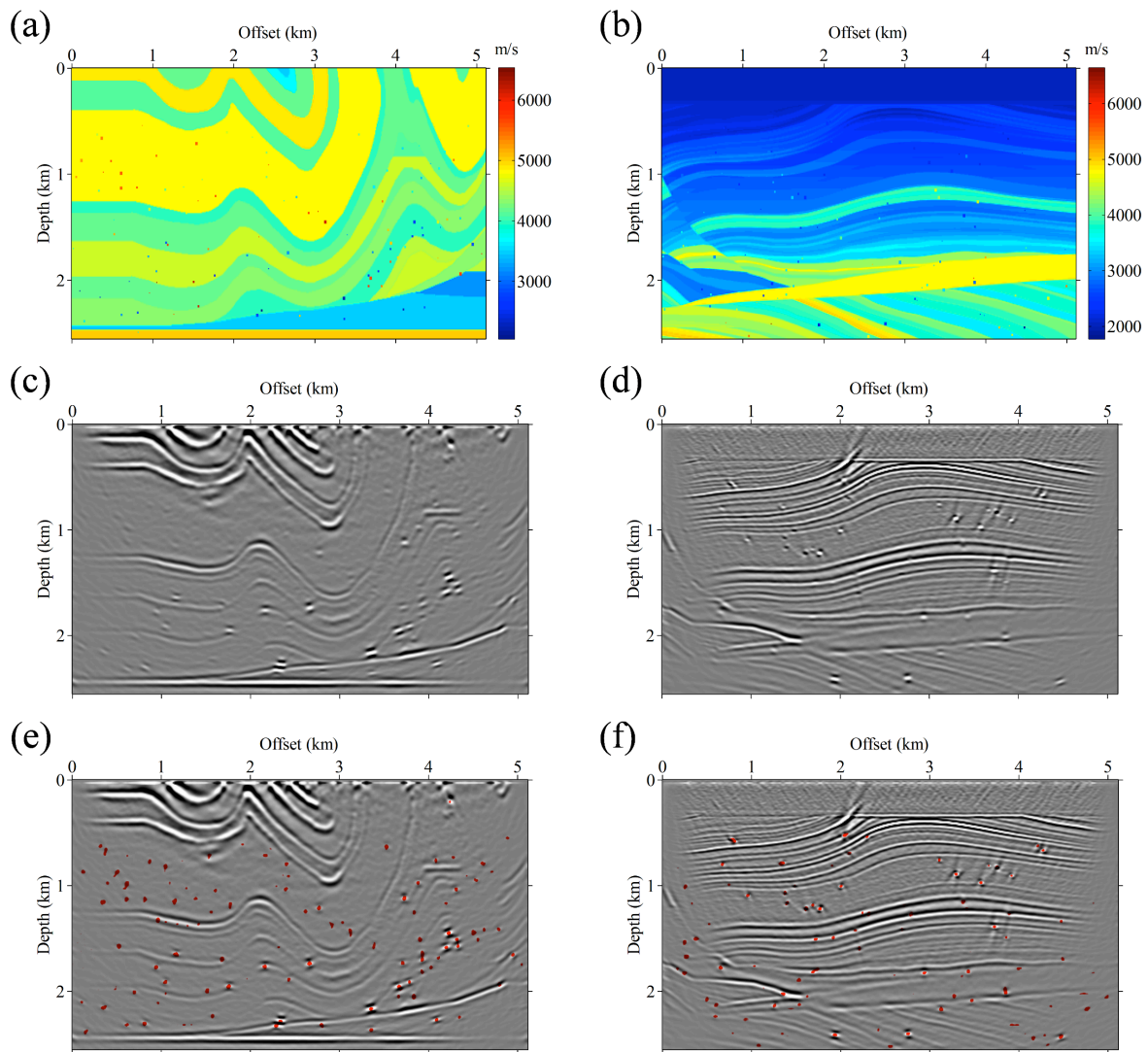


Fig. 9. Sensitivity test on the noisy migration images. The symbols are the same as Fig. 8.

Fig. 9c and Fig. 9d are the imaging results migrated from seismic data in the presence of random noise. The migration noise is obvious and is close to the imaging noise in the field data. We make predictions directly with the trained network, the prediction results are shown as an overlaid image in Fig. 9e and Fig. 9f. The prediction results indicate that our trained network can

be well applied to the imaging results with migration noise, and predict karst caves with high accuracy in locations and scales. For the migration noise similar to the characteristics of beadlike diffractions, the neural network does not mistake them as karst caves. This is reasonable since the migration images in the training data set are generated from shot records with random noise. During the training process, the network learns the difference between migration noise and characteristics of beadlike diffractions, making the trained network less susceptible to noise.

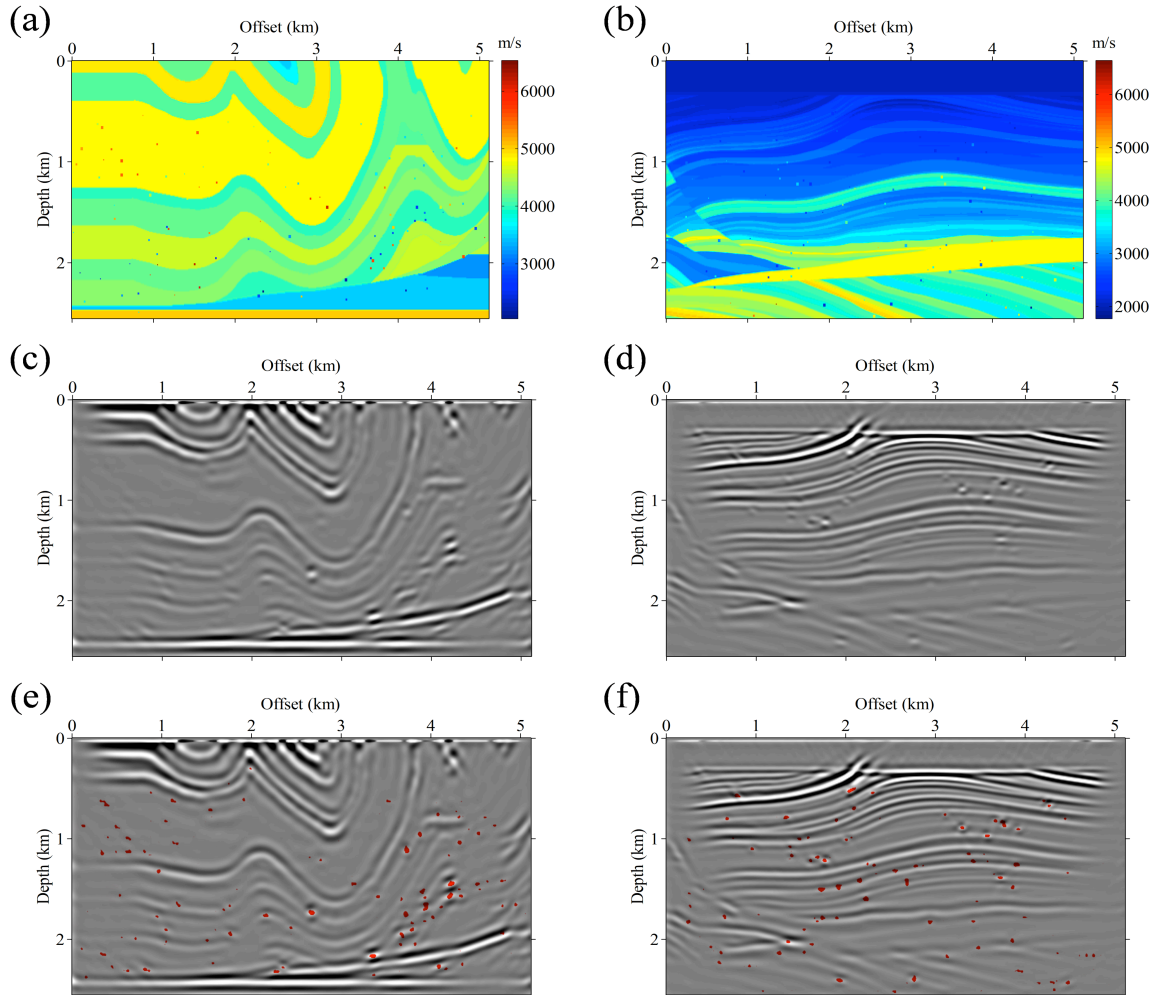


Fig. 10. Sensitivity test on the testing data generated with a 15 Hz Ricker wavelet. The symbols are the same as in Fig. 8.

Considering that the frequencies of different seismic data can be different from each other, we test our network with migration images of

different frequencies to study its sensitivity to wavelet frequency. We generate the new noise free testing data with a 15 Hz Ricker wavelet and the other parameters are the same as those used in the training data generation. The reverse time migration results in Fig. 10c and Fig. 10d show that due to the decrease of frequency, the resolution of imaging results decreases significantly and the seismic events become more blurred. Fig. 10e and Fig. 10f present the prediction results overlaid with the corresponding migration images. It shows that the network can only recognize the karst caves with obvious beadlike diffraction, and the detection accuracy is reduced compared with the prediction results with a Ricker wavelet of 30Hz in Fig. 8e and Fig. 8f. For the beadlike diffraction with weak energy and less obvious characteristics, the trained network can not recognize it as a karst cave well. Those with very weak energy cannot be identified by the neural network or mistakenly identified as karst caves. Though the overall imaging resolution decreases significantly, our trained model can make accurate predictions from the obvious beadlike diffraction energy. This is very important for practical applications because the karst cave velocity in field data is generally different from the surrounding rock velocity, which shows obvious beadlike diffraction characteristics on the imaging profile.

### **Sensitivity tests on inaccurate migration velocity**

We further study the detection performance of the trained network on the migration images with incorrect migration velocity. We apply the trained network to imaging results with different migration velocity errors. Fig. 11a, Fig. 11c, and Fig. 11e are the migration images with migration velocity errors of 0.5%, 1%, and 2%, respectively. Fig. 11b, Fig. 11d, and Fig. 11f are the corresponding prediction results overlaid with migration images. Reverse time migration is sensitive to the accuracy of initial velocity, even a small migration velocity error may lead to inaccurate imaging position of the reflector and on-convergence of energy for small-scale structure in imaging results. However, the trained network shows satisfactory performance in the case of inaccurate migration velocity. Some karst caves with weak imaging energy cannot be identified by the neural network due to the migration velocity errors. For most caves with a large difference in velocity from the surrounding rock, the trained network can still identify them even though their diffraction characteristics are also different from normal.

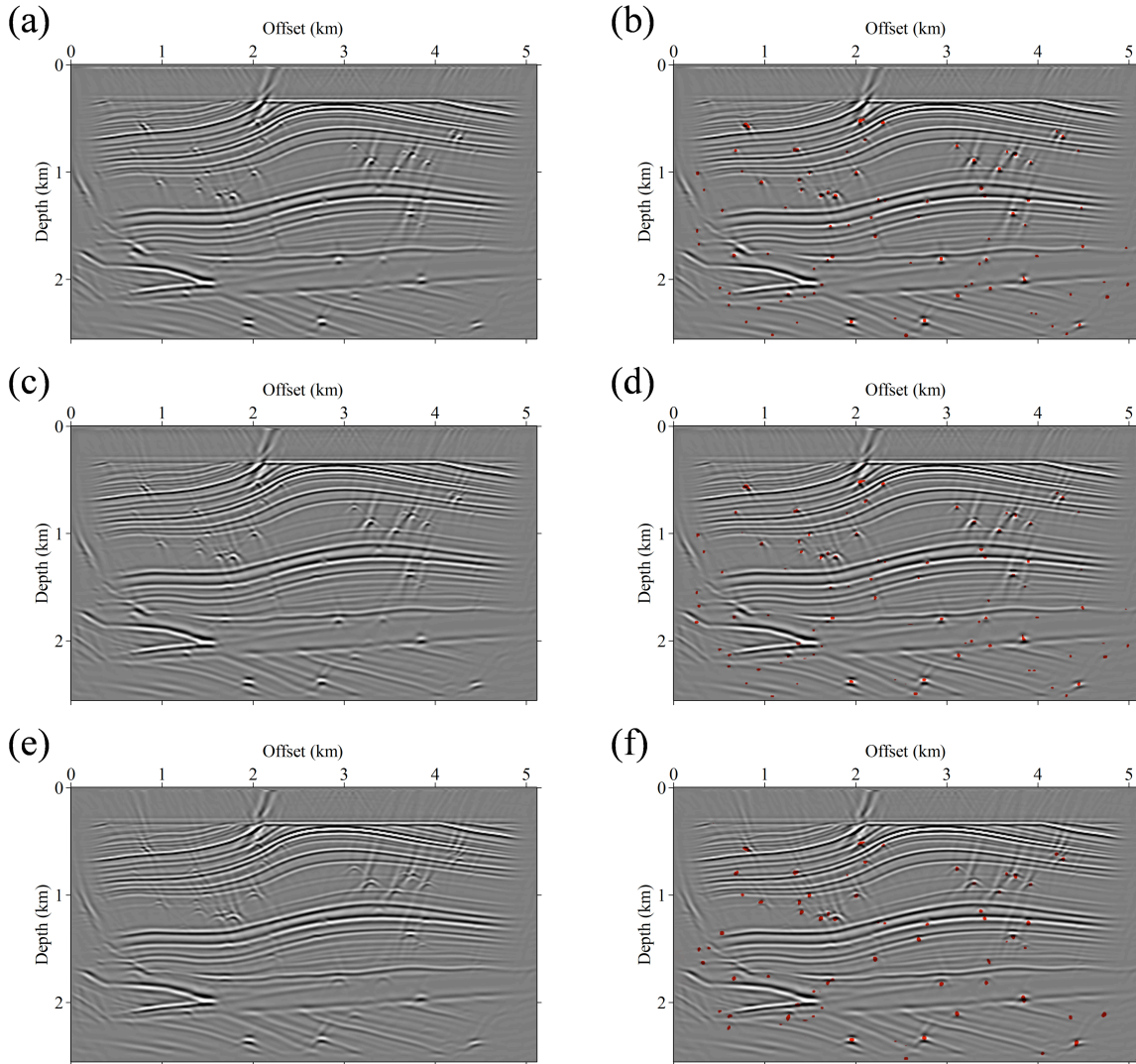


Fig. 11. (a), (c), (e) are the imaging results with migration velocity errors of 0.5%, 1%, and 2%, respectively. (b), (d), (f) are the corresponding prediction results overlaid with migration images.

### Prediction on the physical simulated dataset

To test the applicability of our method in real data, we apply the trained model to a set of physical simulation data. This physical model simulates the ancient river channels and the caves of different scales and depths. The model is made by three-dimensional casting. In areas where cave physics is simulated, small balls made of specific materials are used to simulate karst caves of different sizes. The proposed karst cave identification method is based on the assumption that the karst cave is a cube, and the spherical cave in this physical simulation data is suitable to verify the effectiveness of our method. Fig. 12a is the migration imaging section on the

crossline. It shows that there are three groups of caves placed in sequence from left to right. Fig. 12b is an overlaid display of Fig. 12a and the prediction results. The size and location of almost all karst caves are accurately predicted, and there are no mispredictions. Fig. 13a is the migration imaging profile on the inline. On the left side of the profile, there are a group of karst caves with a gradually deepening buried depth, and some sporadic karst caves are embedded in the cross-section of the ancient channel on the right side. Fig. 13b is an overlay display of the prediction results and the migration image. It indicates that the trained neural network can effectively and accurately predict the karst caves in this geological background.

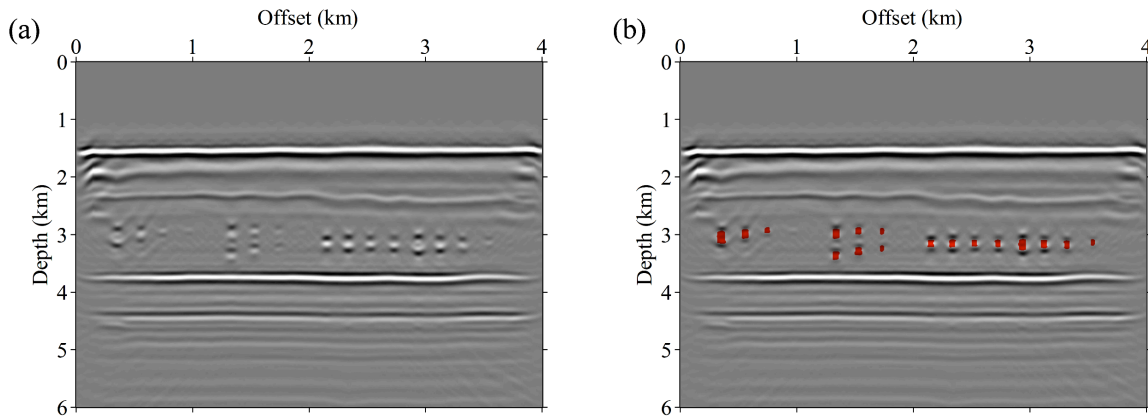


Fig. 12. The migration imaging section of physical simulated data on the crossline. (a) is the migration image. (b) is the overlaid display of (a) and the predicted results.

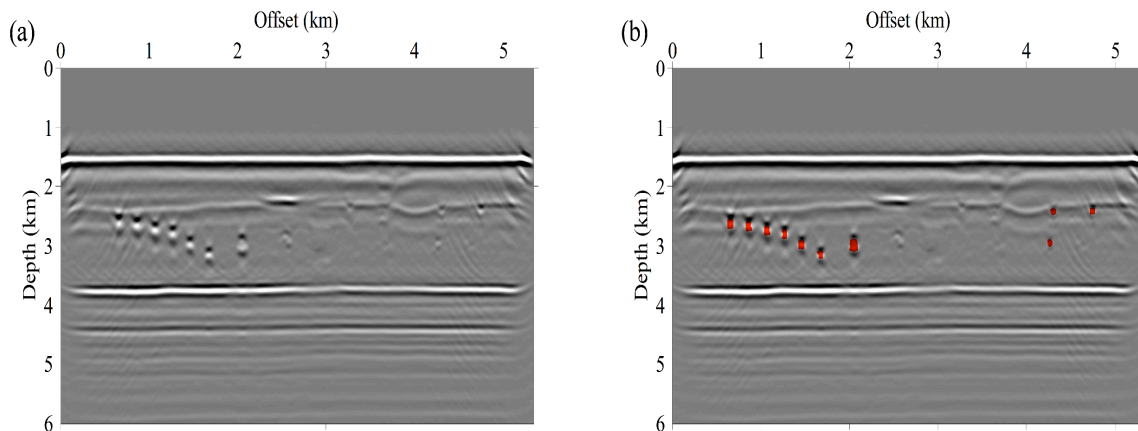


Fig. 13. The migration imaging section of physical simulated data on the inline. The symbols are the same as in Fig. 12.

## DISCUSSION

Through a self-defined modeling method, we generate 55 velocity models with data augmentation and simulate karst caves of different sizes and velocities by adding diffraction points. The seismic records corresponding to these velocity models are generated by the finite difference method with a 30 Hz Ricker wavelet and a grid size of 10 m. Random noise is added to the shot records before performing the migration process. Then the image profiles are derived by reverse time migration. The network takes in the migration imaging profiles and outputs a 2D karst cave distribution probability map. The network shows high performance on the testing data set that are different from the training data set and validation data set. We further study the performance of the karst cave identification of the proposed network with the testing data with poor imaging qualities and different wavelet frequencies. For the data quality sensitivity test, the prediction results with a poor imaging quality are almost accurate as the prediction results with the noise free migration data. This is reasonable because the training data set includes the migration images generated from seismic data with random noise. The neural network learns the difference between migration noise and characteristics of beadlike diffractions during the training process, making it less susceptible to noise. For the input data with a lower wavelet frequency, the prediction accuracy of the trained network is reduced while most of the karst caves can be identified successfully. The smallest size of the karst cave in this grid size, which is  $10 \times 10$  m, can also be correctly identified by the trained network. The main reason for not making the correct identification is that the diffraction features of some karst caves are quite different from those of the training data set, which can be solved by adding these diffraction features to the training data set and transfer learning. The sensitivity test of migration velocity demonstrates that the trained network is less susceptible to the initial velocity error. When the migration velocity error is large, most of the karst caves with obvious characteristics can still be identified.

In practical seismic exploration, the moving acquisition system is usually adopted due to the large distribution of the work area, and the underground karst cave structure mainly presents a vertical beadlike diffraction structure. The training data set generated in this study uses the observation system of full reception on each shot, therefore, the proportion of edge diffraction features is relatively high in the imaging results, which may increase the misidentification rate of the network. Besides, the geometry of the actual underground karst caves is not always regular rectangular. These problems need to be optimized by designing a velocity model similar to the carbonate work area and by designing the karst caves with different geometric shapes to achieve automatic karst cave identification in field data.

## CONCLUSIONS

The detection of karst caves in seismic imaging results generally depends on manually searching for beadlike diffraction features. In this study, we present a convolutional neural network to automatically identify karst caves from 2D migration images. In the data preparation stage, we add diffraction points to the velocity model to simulate the karst caves of different scales and velocities under different geological backgrounds. To improve the recognition effect and simulate the imaging characteristics of different types of karst caves more accurately, we generate the training data sets based on the finite difference method and reverse time migration. We add random noise in the forward simulation to make more realistic migration profiles. Considering that the binary karst cave image is highly imbalanced between ones (karst caves) and zeros (non-karst caves), we use a class-balanced binary cross-entropy loss function to improve the convergence effect of training. The network trained with only 55 synthetic migration images can not only accurately identify the karst caves, but also determine the location and scale of the karst caves with high accuracy. The synthetic tests with a lower wavelet frequency, poor imaging qualities, and incorrect migration velocities demonstrate the capability and stability of our proposed network. Finally, the prediction results on the physical simulated data prove the practicability of our method.

## ACKNOWLEDGEMENTS

This research is supported by the National Key R&D Program of China under contract number 2019YFC0605503C, the Major projects during the 14th Five-year Plan period under contract number 2021QNLM020001, the National Outstanding Youth Science Foundation under contract number 41922028, the Funds for Creative Research Groups of China under contract number 41821002 and the Major Scientific and Technological Projects of CNPC under contract number ZD2019-183-003.

## REFERENCES

- Baysal, E., Kosloff, D.K. and Sherwood, J., 1983. Reverse time migration. *Geophysics*, 48: 1514-1524.
- Berkovitch, A., Belfer, I., Hassin, Y. and Landa, E., 2009. Diffraction imaging by multifocusing. *Geophysics*, 74(6): WCA75-WCA81.
- Burt, P. and Adelson, E.H., 1983. The Laplacian Pyramid as a compact image code. *IEEE Transact. Communicat.*, 31: 532-540.
- Cai, H., Ren, H., Wu, Q. and Hu, G. 2018. Identification of Karst cave reservoirs using optimized convolutional neural network. *Expanded Abstr.*, 88th Ann. Internat. SEG Mtg., Anaheim: 2282-2286.
- Chang, W. and McMechan, G.A., 1987. Elastic reverse-time migration. *Geophysics*, 52: 1367-1375.

- Fan, X., Li, Y. and Zhou, Y., 2017. Fine identification of karst cave based on GST method. SEG Workshop: Carbonate Reservoir: 56-58.
- Gao, Y., Shen, J., He, Z. and Ma, C., 2016. Electromagnetic dispersion and sensitivity characteristics of carbonate reservoirs. *Geophysics*, 81(5): E377-E388.
- Gao, Z., Liu, M., Dang, W. and Cai, Q., 2021. A novel complex network-based deep learning method for characterizing gas-liquid two-phase flow. *Petrol. Sci.*, 18: 259-268.
- Hagedoorn, J.G., 1954. A process of seismic reflection interpretation. *Geophys. Prosp.*, 2: 85-127.
- Hardi, B.I. and Sanny, T.A., 2016. Numerical modeling: Seismic wave propagation in elastic media using finite-difference and staggered-grid scheme. Extended Abstr., 78th EAGE Conf., Vienna.
- He, J., Li, Q., Li, Z., and Lu, X., 2009. Accumulative energy difference method for detecting cavern carbonate reservoir by seismic data. *Geophys. Prosp. for Petrol.*, 48: 337-341.
- Huang, W., Gao, F., Liao, J. and Chuai, X., 2021. A deep learning network for estimation of seismic local slopes. *Petrol. Sci.*, 18(6): 92-105.
- Khaidukov, V., Landa, E. and Moser, T., 2004. Diffraction imaging by focusing-defocusing: An outlook on seismic superresolution. *Geophysics*, 69: 1478-1490.
- Kingma, D. and Ba, J., 2014. Adam: a method for stochastic optimization. arXiv preprint arXiv:1412.6980.
- Krey, T., 1952. The significance of diffraction in the investigation of FAULTS. *Geophysics*, 17: 843-858.
- Kong, X., Wang, D., Li, Z., Zhang, R. and Hu, Q., 2017. Diffraction separation by plane-wave prediction filtering. *Applied Geophysics*, 14(3): 399-405.
- Liu, Z., Song, C., Li, Z., Yao, X. and Hu, G., 2016. Multi-attribute fusion based level sets for caves segmentation. Expanded Abstr., 86th Ann. Internat. SEG Mtg., Dallas: 1919-1923.
- Nair, V. and Hinton, G.E., 2010. Rectified Linear Units Improve Restricted Boltzmann Machines. Internat. Conf. Machine Learning: 807-814.
- Özdenvar, T. and McMechan, G.A., 1997. Algorithms for staggered-grid computations for poroelastic, elastic, acoustic, and scalar wave equations. *Geophys. Prosp.*, 45: 403-420.
- Qu, S., Zhu, S. and Zhao, Q., 2012. Analysis of seismic reflection characters for carbonate Karst reservoir. *Chin. J. Geophys.* (in Chinese), 55: 2053-2061.
- Ronneberger, O., Fischer, P. and Brox, T., 2015. U-Net: Convolutional networks for biomedical image segmentation. Internat. Conf. Medical Image Computing and Computer-Assisted Intervention: 234-241.
- Shen, H., Li, Q., Yan, Y., Li, X. and Zhao, J., 2020. Separation of diffracted waves via SVD filter. *Petrol. Sci.*, 17: 1259-1271.
- Shi, Y., Wu, X. and Fomel, S., 2018. Automatic salt-body classification using a deep convolutional neural network. Expanded Abstr, 88th Ann. Internat. SEG Mtg., Anaheim: 1971-1975.
- Silvestrov, I., Baina, R. and Landa, E., 2016. Poststack diffraction imaging using reverse-time migration. *Geophys. Prosp.* 64: 129-142.
- Wang, Y., Lu, W., Wang, B., Chen, J. and Ding, J., 2017. Extraction of strong beadlike reflections for a carbonate-karst reservoir using a tensor-based adaptive mathematical morphology. *J. Geophys. Engineer.*, 14: 1150-1159.
- Wang, Z., Wang, R., Weger, R.J., Li, T. and Wang, F., 2015. Pore-scale modeling of elastic wave propagation in carbonate rocks. *Geophysics*, 80(1): D51-D63.
- Wu, X., Liang, L., Shi, Y. and Fomel, S., 2019. FaultSeg3D: Using synthetic data sets to train an end-to-end convolutional neural network for 3D seismic fault segmentation. *Geophysics*, 84(3): IM35-IM45.

- Xie, S. and Tu, Z., 2015. Holistically-nested edge detection. *Internat. Conf. Comput. Vision*: 1395-1403.
- Xu, C., Di, B. and Wei, J., 2016. A physical modeling study of seismic features of karst cave reservoirs in the Tarim Basin, China. *Geophysics*, 81(1): B31-B41.
- Yang, F. and Ma, J., 2019. Deep-learning inversion: A next-generation seismic velocity model building method. *Geophysics*, 84(4): R583-R599.
- Zhu, X. and Wu, R.S., 2010. Imaging diffraction points using the local image matrices generated in prestack migration. *Geophysics*, 75(1): S1-S9.